



Evaluation of the CMIP6 planetary albedo climatology using satellite observations

Bida Jian¹ · Jiming Li¹ · Yuxin Zhao¹ · Yongli He¹ · Jing Wang¹ · Jianping Huang¹

Received: 16 November 2019 / Accepted: 25 April 2020
© Springer-Verlag GmbH Germany, part of Springer Nature 2020

Abstract

The Earth's planetary albedo (PA) has an essential impact on the global radiation budget. Based on 14 years of monthly data from the Clouds and the Earth's Radiant Energy System energy balanced and filled (CERES-EBAF) Ed4.1 dataset and atmosphere-only simulations of the Coupled Model Intercomparison Project Phase6 (CMIP6/AMIP), this study investigates the ability of CMIP6/AMIP model in reproducing the observed inter-month changes, annual cycle and trend of PA at near-global and regional scales. Statistical results indicate that some persistent biases in the previous models continue to exist in the CMIP6 models; however, some progresses have been made. In CMIP6/AMIP, large negative correlations for PA between the model ensemble mean and observation are addressed over the subtropical stratocumulus regions. In addition, the simulation of PA in drylands and tropical oceans remains a challenge in CMIP6 models. Over the most regions, PA biases are governed by cloud albedo forcing biases. These results demonstrate the importance of improving cloud process simulations for accurately representing the PA in models. For the annual cycles, the model ensemble mean captures the difference in amplitude between the two peak values of PA (June and December), as well as the phase of the seasonal cycle, despite PA is systematically overestimated. The differences between different terrestrial climatic regions are also examined. Results indicate that the relative biases of PA are greatest in semi-arid (2.2%) and semi-humid (2.8%) regions, whereas the minimum relative bias occurs in arid regions (0.3%) due to compensating errors.

Keywords Planetary albedo · CMIP6 · Satellite observations

1 Introduction

The planetary albedo (PA) is defined as the percentage of incident sun's energy reflected back to space by the Earth-atmosphere system (Pallé et al. 2004). As a crucial variable of the global energy budget, PA determines how much solar energy is absorbed and distributed by the Earth (Fu et al. 2000; Stephens et al. 2015). Any slight perturbation in the PA could be sufficient to counteract the additional radiative forcing caused by greenhouse gases (Houghton et al. 2001). Thus, it is necessary to know the basic statistical properties

of PA and understand the processes that govern its distribution, magnitude and long-term variations at global and even regional scales.

Currently, general circulation models (GCMs) are powerful tools to understand the present climate and forecast future climate change (Stocker et al. 2013; Wang and Su 2013). If GCMs can reproduce the basic statistical properties of the historical PA, it is bound to enhance our confidence in projecting future PA variations and reducing the uncertainty in climate predictions. Nevertheless, due to the insufficient understanding of inherent physical mechanisms and key control variables, there are still large discrepancies in PA between models and observations (or models) (Bender et al. 2006; Lauer and Hamilton 2013; Stephens et al. 2015). For example, Bender et al. (2006) compared the multimodel ensemble outputs from Coupled Model Intercomparison Project Phase 3 (CMIP3) historical runs and satellite observations. They found that the simulated global mean albedo is systematically higher than those values from observation, and models usually overestimate and underestimate

Electronic supplementary material The online version of this article (<https://doi.org/10.1007/s00382-020-05277-4>) contains supplementary material, which is available to authorized users.

✉ Jiming Li
lijiming@lzu.edu.cn

¹ Key Laboratory for Semi-Arid Climate Change of the Ministry of Education, College of Atmospheric Sciences, Lanzhou University, Lanzhou, China

albedo during boreal summer and winter, respectively. The obvious overestimation during boreal summer months even persists to CMIP5 and reaches 10% (Stephens et al. 2015). More importantly, the CMIP5 models still cannot reproduce the observed hemispheric symmetry in PA (Stephens et al. 2015), even though considerable efforts have been made in improving important physical processes and increasing the perfection of the models (Van Weverberg et al. 2018). Satellite records have indicated that the global annual mean albedo maintains a relatively stable value (approximately 0.29) (Bender et al. 2006), and this stability started in the Holocene (Houghton et al. 2001). Therefore, models' inability to capture the hemispheric symmetry of PA possibly originate from the fact that models cannot accurately simulate the components of PA (i.e., atmospheric and surface albedos) and quantify their respective contributions to PA variability, especially on the local scale (Stephens et al. 2015; Van Weverberg et al. 2018). Indeed, by analyzing albedo simulations from the CMIP3 multimodel dataset and observation from Clouds and the Earth's Radiant Energy System (CERES) satellite dataset, Donohoe and Battisti (2011) found that atmospheric reflection dominates globally averaged PA (88%). The contribution of surface albedo (SA) is small because the atmosphere attenuates the surface contribution by a factor of approximately 3. Thus, the discrepancies of atmospheric radiation processes in models may be the main factor of the large intermodel spread of PA (Donohoe and Battisti 2011).

Regional PA has been proven to be highly changeable with local surface and cloud properties (such as: cloud cover, snow cover and vegetation), which exhibit significant spatiotemporal variations (Hu and Stammes 1993, 2000; Loeb et al. 2007; Voigt et al. 2014; Letu et al. 2018; Li et al. 2018; Zhao et al. 2019; Yang et al. 2020) and induce large uncertainty in simulating and predicting the regional PA (Pallé et al. 2004; Bender et al. 2006; Solomon et al. 2007; Lauer and Hamilton 2013; Donohoe and Battisti 2011). Although the regional biases in simulated PA possibly cancel each other out when calculating the hemispheric or global mean albedos, this issue should be further quantitatively assessed for improving the calculation of the regional energy budget and reducing uncertainty in regional climate prediction, in particular, over those regions that have experienced significant climate change over the past decades due to frequent human activity (e.g., semi-arid regions, Huang et al. 2016a, b). Satellite observations allow us to perform a systematic comparison between simulated and observed PA, including not only the magnitude of the PA bias but also its annual cycle and long-term variability over a special region (Qu and Hall 2005; Bao et al. 2018; Zhao et al. 2019). Although there are some potential uncertainties in satellite observation due

to the limited revisiting time, the errors of time representation can be very small after averaging long-term satellite observation (Wang and Zhao 2017). Recently, the latest climate model intercomparison project (i.e., CMIP6) (Eyring et al. 2016) provides us with an excellent chance to assess the ability of current climate models to simulate PA using satellite observation data, and to further understand what progress has been achieved in the last ten years.

Here, this study combines 14 years (2001–2014) of the monthly CERES albedo dataset and eighteen CMIP6 AMIP simulation outputs to analyze the near-global and regional biases of the simulated PA. In AMIP-type simulations, the same atmospheric models as coupled CMIP6 simulations are employed, but the sea ice concentrations and sea surface temperatures (SSTs) are the same as the observations (Eyring et al. 2016). This means that AMIP simulations are ideal tools to study the sensitivity of atmospheric responses and model deficiencies because AMIP can well represent the important coupled atmosphere–ocean variability related to SST, e.g., the El Niño–Southern Oscillation (ENSO) signature; therefore the AMIP simulated atmospheric state and surface heat fluxes are not affected by model biases caused by SST differences (Wang and Su 2013; Fan et al. 2018b). In the following study, our main aim is to assess the capability of CMIP6/AMIP climate models in reproducing the observed planetary albedo using satellite observations. In particular, we pay more attention to analyze the potential differences in different terrestrial climatic regions and address three key points: First, whether the current GCMs can reproduce the inter-month variation and annual cycle of planetary albedo? Second, how does the bias of simulated PA change with climatic regions? Finally, can the model outputs capture the trends of observed PA and the relative contributions of cloud and surface albedo anomalies to the long-term variation in PA?

This paper is arranged as follow: dataset and method are provided in Sect. 2. In Sect. 3.1, we assess the seasonal and annual biases of simulated near-global and regional planetary albedos, and further examine the inter-month variability and annual cycle of simulated PA. The results and analysis of model uncertainty in different climatological regions and the trend biases of PA are presented in Sects. 3.2, 3.3. Finally, the conclusions and discussion are provided in Sect. 4.

2 Datasets and method

Fourteen years (2001–2014) of data from the CERES EBAF 4.1 dataset and eighteen CMIP6/AMIP simulations are collected to evaluate the near-global (e.g., between 60° S and 60° N) and regional bias of the simulated PA.

2.1 CERES

The CERES EBAF radiation product can provide long-term radiation data at the top of atmosphere (TOA) and surface at a global scale, which is widely used in many studies (Xie et al. 2013; Loeb et al. 2016). The CERES instrument onboard the polar-orbiting satellites Aqua and Terra can accurately measure the global TOA shortwave (SW) radiances (Doelling et al. 2013). Then, the radiances are converted into instantaneous TOA radiative fluxes by employing the empirical angular dependence models (Doelling et al. 2013). Different from the TOA fluxes, surface fluxes are computed based on a radiative transfer model by using reanalysis meteorological data (i.e., temperature and specific humidity) and cloud and aerosol properties derived from satellite (Kato et al. 2018). Compared to previous versions, Ed4.1 provides new clear-sky TOA and surface fluxes, which are determined for the entire region instead of cloud-free portions of a region. These new clear-sky fluxes are more consistent with the way the clear-sky fluxes are expressed in the climate model. Details about the new clear-sky fluxes can be found in the CERES_EBAF_Ed4.1 Data Quality Summary (2019). In the following analysis, the TOA outgoing SW flux (all-sky), TOA outgoing SW flux (clear-sky for the entire region) and TOA incoming SW flux are used to calculate the PA, the clear-sky PA and the corresponding cloud albedo forcing (see Sect. 2.4). Meanwhile, the surface reflected and incident SW fluxes (clear-sky for the entire region) are used to calculate the surface albedo. The horizontal resolutions of the above products are $1^\circ \times 1^\circ$.

2.2 CMIP6/AMIP

Eighteen models of CMIP6 projections that have AMIP simulations (from January 1979 through December 2014) are used in the study. Note that only the first ensemble member (“r1i1p1f1”) is used for each model. However, other ensemble members are considered if the first ensemble member is unavailable (e.g., CNRM-CM6, CNRM-ESM2-1 and UKESM1-0-LL (“r1i1p1f2”), HadGEM3-GC31-LL (“r1i1p1f2”)). Relevant details of the eighteen models are given in Table S1. Similar to the CERES product, monthly averaged all-sky PA, clear-sky PA, cloud albedo forcing and surface albedo during 2001–2014 are calculated based on the simulated downward and upward fluxes for each model and their ensemble mean (MEM). To match the CERES resolutions, all model outputs are regressed to $1^\circ \times 1^\circ$.

2.3 Aridity index

To assess the capability of the GCM in simulating PA over the different climatological regions (especially over landmass), the aridity index (AI) is applied to divide the global

landmass into different climatological types. Here, the AI represents the drought degree of a given land region and is expressed as the percentage of the annual precipitation to annual potential evapotranspiration (P/PET) (Middleton and Thomas 1997). In the following study, the validated AI dataset (1978–2008), with a spatial resolution of $0.5^\circ \times 0.5^\circ$, is used based on the study of Feng and Fu (2013), who computed PET by applying a superior, physically-based PET algorithm, i.e., the Penman–Monteith algorithm, which considers the responses to meteorological factors (e.g., humidity and winds) (Maidment 1993; Fu and Feng 2014). Finally, five land types are divided on the basis of the AI: hyper-arid regions ($AI < 0.05$), arid regions ($0.05 \leq AI < 0.2$), semi-arid regions ($0.2 \leq AI < 0.5$), semi-humid regions ($0.5 \leq AI < 0.65$) and humid regions ($0.65 \leq AI$).

2.4 Methodologies

In this study, the near-global (or regional) averaged albedo $\bar{\alpha}_k$ in the given region k is calculated as follows (Huang et al. 2012):

$$\bar{\alpha}_k = \frac{\sum_{i=1}^{N_k} W_{ki} \cdot \alpha_{ki}}{\sum_{i=1}^{N_k} W_{ki}} \quad (1)$$

where N_k is the grid sample numbers of area k and α_{ki} is the corresponding albedo of the grid i in this area. In addition, $W_{ki} = \cos(\theta_i \cdot \pi/180.0)$, where θ_i is the grid's latitude. Meanwhile, the regional means of other variables are also calculated based on the similarly weighted equation.

Also, the cloud albedo forcing (CAF) may be written as: $CAF = PA - (\text{clear-sky PA})$. Note that some aerosol effects are also included in CAF (Zhao et al. 2012; Jian et al. 2018). Following Stephens et al. (2015), we use the root mean square (RMS) of the deseasonalized monthly albedo anomalies (i.e., the standard deviation of albedo anomalies) to quantify the inter-month variability of variables. Here,

$$RMS = \sqrt{\frac{\sum_{x=1}^n (\Delta\alpha)^2}{n}} \quad (2)$$

where $\Delta\alpha$ are the deseasonalized monthly albedo anomalies ($n = 168$).

Because the CAF and surface albedo govern the PA change, the PA change may be expressed using a linear regression model as (Jian et al. 2018):

$$\Delta\alpha_{all} = \frac{\partial\alpha_{all}}{\partial\alpha_{cloud}} \cdot \Delta\alpha_{cloud} + \frac{\partial\alpha_{all}}{\partial\alpha_{surface}} \cdot \Delta\alpha_{surface} + c \quad (3)$$

where $\Delta\alpha_{all}$, $\Delta\alpha_{cloud}$ and $\Delta\alpha_{surface}$ are the PA, CAF and surface albedo anomalies, respectively. The constant

term c represents the residual PA anomaly that cannot be explained by either CAF or surface albedo anomalies.

Further, to understand the error sources of simulated PA, we calculate the relative contribution rates of $\Delta\alpha_{\text{cloud}}$ and $\Delta\alpha_{\text{surface}}$ to $\Delta\alpha_{\text{all}}$ based on Eq. (4):

$$R_j = \frac{1}{m} \sum_{i=1}^m \left[T_{ij}^2 / \left(\sum_{j=1}^2 T_{ij}^2 \right) \right] \quad (4)$$

where m is the length of the data series. $T_{ij} = b_j x_{ij}$, where b_j indicates the corresponding regression coefficients of individually variable which is based on Eq. (3), x_{ij} represents the predictor variables (Huang and Yi 1991).

3 Results

3.1 Evaluation of seasonal and inter-month variabilities of albedo based on observation

In the Fig. 1a–o, we first evaluate the climatological spatial patterns of the seasonal and annual averaged planetary albedos from multimodel ensemble mean (MEM) based on satellite observations. Generally, observation and MEM exhibit similar near-global distributions of PA (Fig. 1a–j), however, the differences between MEM and observation are still significant among seasons and regions. Figure 1k–o show that MEM significantly underestimates the PA over those typical stratocumulus regions (e.g., off the coast of Namibia and the Canary Islands) and southeast part of China, where the PA bias even reaches -0.1 . The obvious underestimations over these regions could not be caused by the bias of surface

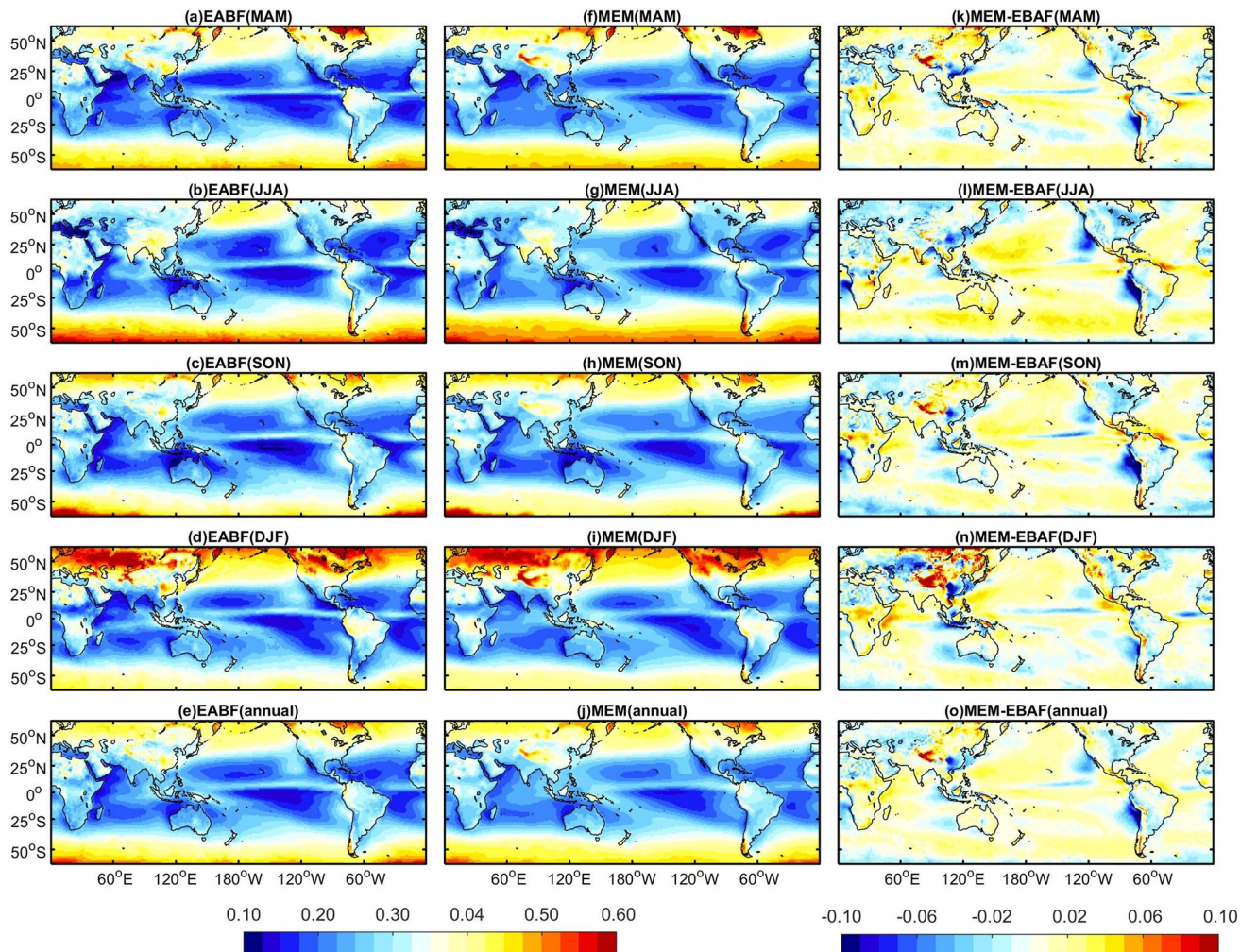


Fig. 1 Near-global distributions of seasonal and annual mean climatology of PA for **a–e** satellite observed, **f–j** multimodel ensemble mean simulated and **k–o** the difference between MEM and EBAF

albedo or water vapor (or aerosol) simulation in models, because we also perform similar comparisons between MEM and observation for clear-sky PA (see Fig. S1) and surface albedo (see Fig. S2), and find that the MEM shows weak bias and thus has a good consistency with observation in simulating the clear-sky PA over the vast ocean. Further, we compare the seasonal and annual CAF differences between the MEM and CERES (see Fig. S3), and find that the large negative biases in simulated CAF over the subtropical stratocumulus regions and southeast part of China match the underestimates of PA. Meanwhile, the moderate positive biases of CAF are widely distributed in the other ocean regions, particularly over the intertropical convergence zone (ITCZ), the central subtropical Pacific and the Atlantic Ocean and the tropical Indian Ocean. The spatial distribution of CAF difference is also very similar to those of PA difference. These results mean that the representations of cloud properties related with CAF (e.g., cloud fraction and cloud albedo) in models still suffer from large uncertainty, thus possibly contribute to the most of the bias of PA simulation over the above regions. Indeed, some studies have indicated that the absorbing aerosols from biomass burning can be transported to subtropical stratocumulus regions and overlying the cloud layer (Wilcox 2010; Xu et al. 2017), thereby strongly influence the cloud albedo and its simulation. Based on the CMIP5 outputs and satellite observation, Bender et al. (2016) have verified that the large bias of cloud albedo simulation exists over these stratocumulus regions, and attributed the bias to the inability of climate models in simulating aerosol-cloud interaction (Fan et al. 2018a, b). In addition, a recent study suggested that the cloud fraction simulation is still problematic in CMIP6 models (Vignesh et al. 2020). Similar with the study based on CMIP5/AMIP models from the Wang and Su (2013), we also evaluate the SW cloud radiation forcing (CRF, the difference of TOA shortwave radiation between clear-sky and all-sky conditions, CRF less than zero indicate cooling effect) instead of cloud albedo forcing (see Fig. S4), and find that overestimations of cloud cooling effect (negative biases) over the tropical oceans and considerable underestimations of cloud cooling effect (positive biases) over the subtropical stratocumulus region persist from CMIP5 to CMIP6. The biases of CRF and PA over the stratocumulus regions refer to the simulation of low-level cloud properties, however, Nam et al. (2012) found that the CRF bias over the tropical oceans is largely associated with simulated stronger tropical convection (overly brighter clouds).

Based on Fig. 1 and Figs. S1–S3, we also find that MEM tends to underestimate the CAF during boreal cold season and continuously overestimate the clear-sky PA (or surface albedo) over the Tibetan plateau (TP), the dominant bias from clear-sky PA results in the simulation of PA over the TP region is still overestimated, especially during the boreal

winter (December–February (DJF)). However, it is also noteworthy that satellite retrieval of cloud properties over the TP still suffers from large uncertainty (Zhao et al. 2019), it may cause potential uncertainty in surface radiation data and bias our statistical results. In Fig. S2, it is clear that large surface albedo bias is also particularly evident over other arid or semi-arid regions (e.g., central Asia and western part of North America) of northern hemisphere during winter season. The obvious underestimation of PA over central Asia is clearly related to the surface albedo bias in models, and persistently exists from CMIP5 to CMIP6. For example, based on CMIP5 coupled historical output, a previous study has shown that the biases in snow cover and the difference between snow-covered and snow-free albedo (DSA) during boreal winter contribute most to the bias in surface albedo over central Asia, the northwestern part of North America and the TP (Li et al. 2016). Over the boreal forests (such as Siberia), the large positive bias of the DSA and the lower leaf area index (LAI) simulation dominates the positive bias in surface albedo, thus result in the overestimation of PA over this region (Li et al. 2016). These results suggest that the new generation GCMs continue to be challenged in simulating the multiyear annual mean surface albedo over dryland areas (i.e., arid and semi-arid regions). Further considerations about the snow cover, DSA and vegetation cover parameterization are needed to improve the surface albedo representation and subsequent clear-sky albedo.

Figures 2a–c displays the near-global distributions of temporal correlations between the MEM simulated and CERES observed PA, clear-sky PA and CAF, respectively. Bender et al. (2006) noted that the correlations between the simulated and observed time series of albedo are dominated by strong seasonal cycles. We can see that the models simulate the clear-sky PA well at the near-global scale (Fig. 2a), except in the central parts of Africa and South America, where the correlations exhibit weak and even negative values. This may because the models have difficulties in reproducing the clear-sky PA seasonal cycle in those regions with weak seasonal cycles (see Fig. 5a). The poor simulation of clear-sky PA over central Africa is likely to be associated with several processes, including land cover change, biomass burning aerosol emissions and its absorption effect, which further impact the seasonal cycles of surface albedo and atmospheric transmittance there (Govaerts et al. 2002; Myhre et al. 2008; Ichoku et al. 2016). For CAF (Fig. 2b), weak correlations (< 0.4) can be found in some typical drylands (e.g., North Africa, Central Asia, the TP and Australia) and over the most part of oceans, particularly in the Southern Ocean, indicating that the cloud properties simulation is poor over these regions. A previous study has noted that the model discrepancies in representing the mixed-phase cloud result in the difference of the cloud albedo forcing response in the models (Tsushima et al. 2006). The improvement of

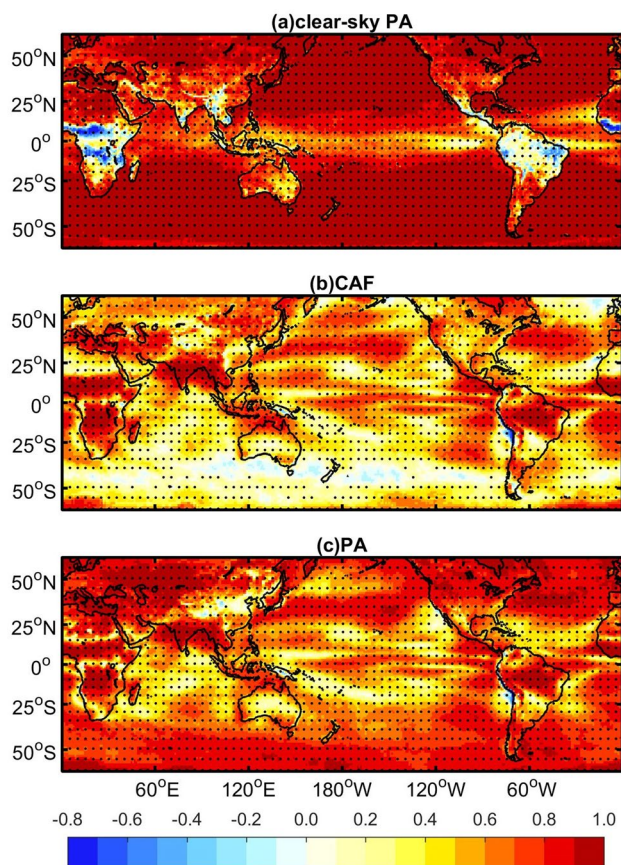


Fig. 2 Near-global distributions of the **a** clear-sky PA, **b** cloud albedo forcing and **c** PA temporal correlations between multimodel ensemble mean and CERES observations from 2001 to 2014. Monthly mean data for 14 years are used to calculating the correlation coefficient. Dotted regions indicate that the correlations are significant at the 95% confidence level

the mixed-phase cloud or supercooled water cloud parameterizations may reduce above bias over the Southern Ocean (McCoy et al. 2015; Li et al. 2017). The subtropical stratocumulus regions are the typical regions where models struggle to reproduce the observations (Lauer et al. 2017). Previous studies also noted that the poor simulation of low clouds over these regions had not changed in the CMIP5 (Boucher et al. 2013; Lauer and Hamilton 2013). Compared with CMIP3 coupled model simulations (Bender et al. 2006), however, our results indicate that the large negative correlations of PA over the subtropical stratocumulus regions have changed to moderate positive correlations in CMIP6 AMIP. To check whether the SSTs simulations will affect the results, we compare the results of the CMIP6 AMIP with the simulations of the coupled model, and find that the near-global distribution patterns of the temporal correlations and annual mean biases are very similar in the AMIP and coupled model simulations (not shown), indicating that the AMIP simulations do not outperform the CMIP simulations in simulating PA seasonal

cycles. These results indicate that the performance in reproducing the observed PA seasonal cycle in subtropical stratocumulus regions is improved slightly in CMIP6.

Figure 3a–c further shows the near-global distribution of temporal correlations between the MEM simulated and CERES observed PA, clear-sky PA and CAF anomalies, respectively. Note that all data are deseasonalized (i.e., the seasonal cycle is removed). Figure 3b and c show similar spatial distribution because the changes of PA are governed by the variations in cloud properties (Jian et al. 2018). It indicates that the improvement of CAF anomalies simulation is key to reproduce the long-term changes of PA. The insignificant correlations over the majority of land regions verify the difficulty of models in reproducing the inter-month variations of PA. Same as the Fig. 3a–e exhibits the performance of the individual model in reproducing the time series of the near-global averaged clear-sky PA, CAF and PA anomalies. Figure 3d clearly shows that the correlations for three variables are weak (< 0.4) for all models. For the PA, CNRM-CM6-1 is more agreement with CERES EBAF, and BCC-ESM1 is the least comparable with CERES EBAF. The correlation coefficients of clear-sky PA range from -0.18 to 0.24, and exhibit a larger intermodel spread than those of CAF and PA, it mainly because the models vary greatly in simulating inter-month variability of clear-sky PA. Additionally, we find that the MEM generally has better agreement with the observations for CAF and PA compared with individual models, which is in agreement with earlier studies (Gleckler et al. 2008). The above results indicate that the simulation of inter-month variation of PA remains a challenge in CMIP6 models, which is persisted from CMIP3 (Bender et al. 2006). The observed inter-month variations of CAF and PA are very similar (Fig. 3e and Fig. S5). Most of the models can capture the feature and reproduce the observed near-global averaged inter-month variability of PA. For the PA, twelve of the 19 models exhibit stronger near-global averaged inter-month variation compared to the observation. In contrast, CESM2 and CESM2-WACCM produce much stronger variations than CERES EBAF and other models, while CanESM5 is the most comparable with CERES EBAF. However, the simulated inter-month variability of PA by MEM is much smaller than those from the observation and individual models. To investigate the causes of this bias, we check the spatial distribution of inter-month variability for clear-sky PA, cloud albedo forcing and PA based on MEM and satellite observations (see Fig. S5). The statistical results indicate that the simulated inter-month changes of clear-sky PA, CAF and PA over the most of regions are very weak compared to the observations, which may due to the compensation effect after multi-model averaging.

Further, Fig. 4a–c compares the 14-year averaged annual cycles of clear-sky PA, CAF and PA from the

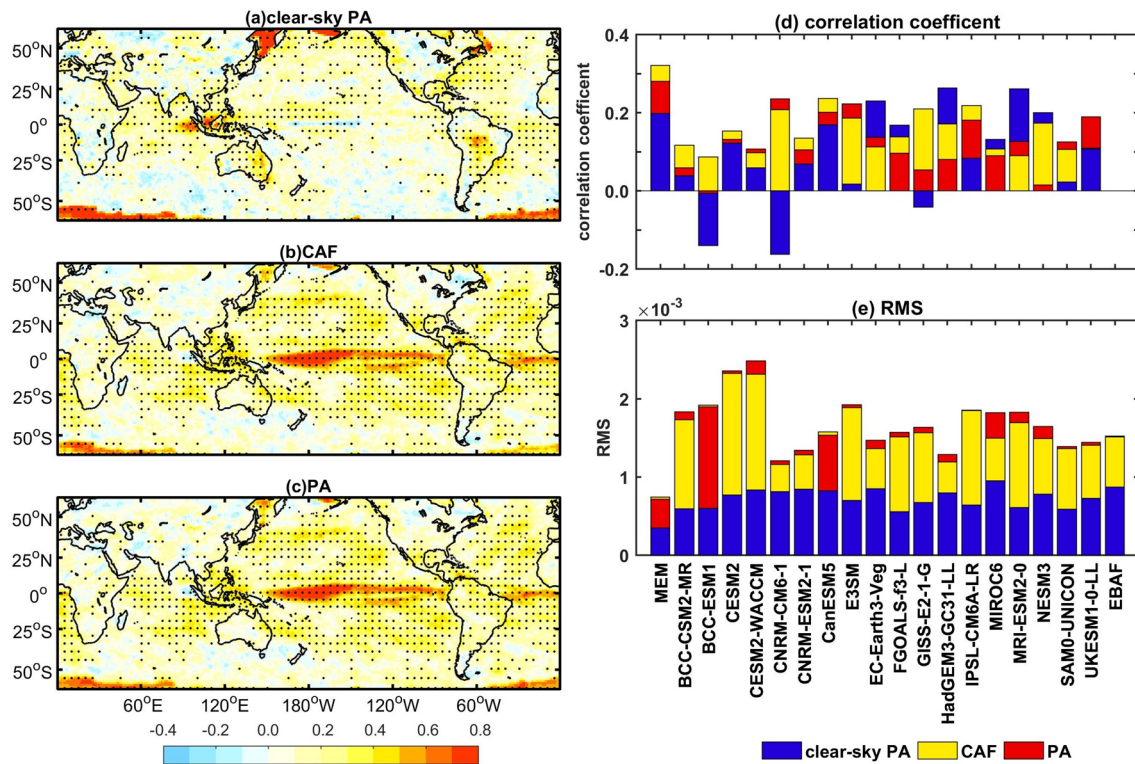


Fig. 3 Near-global distributions of the temporal correlations of the **a** clear-sky PA, **b** cloud albedo forcing and **c** PA anomalies between multimodel ensemble mean and CERES observations from 2001 to 2014. The temporal correlations and inter-month variability of the clear-sky PA, cloud albedo forcing and PA for different models and

observations are provided in the right panel (**d** and **e** subplots). Here, monthly deseasonalized data for 14 years are used to calculate the correlation coefficient. Dotted regions indicate that the correlations are significant at the 95% confidence level

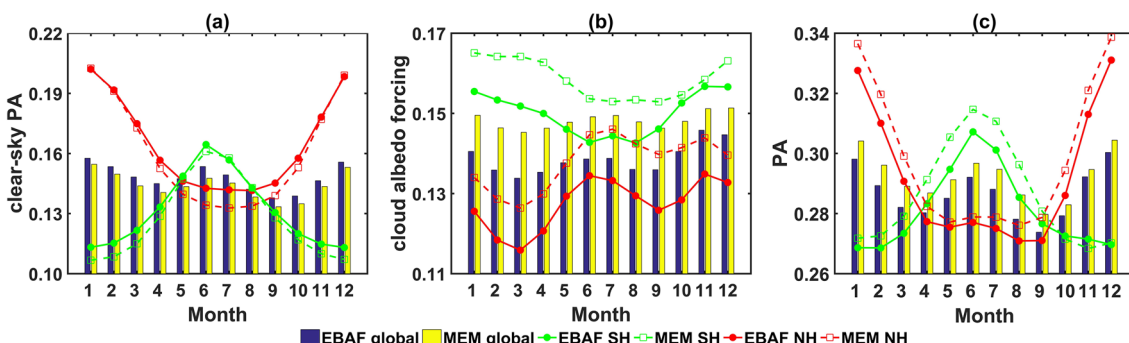


Fig. 4 Annual cycles of **a** clear-sky PA, **b** cloud albedo forcing and **c** PA for near-global (blue (CERES EBAF) and yellow (MEM) bars), SH (green lines), NH (red lines). The solid lines show the results

from satellite observations, the dash lines show the results from multimodel ensemble mean

MEM with that of satellite observations on the near-global and hemisphere scales. It is clear that the observed annual cycle of the near-global average PA has obvious double peaks (Fig. 4c). It reaches the maximum in June and December due to the tilt of the Earth's axis (Loeb et al. 2007). Although the present study excludes the polar region, the temporal variations in PA are still likely to

be related to the variations in snow/ice cover at the middle latitudes. However, the observed annual cycles of the two hemispheric averaged PAs both have a single-peak structure. The peak value in the NH occurs in December, whereas that in the SH occurs in June. The peak value of the NH is approximately 0.02 higher than that of the SH, resulting in a higher peak of the near-global averaged

PA during boreal winter. These results are consistent with the previous study from Bender et al. (2006) and Loeb et al. (2007). Compared with the observation, the annual cycle of near-global averaged PA is well reproduced by the model. The model tends to systematically overestimate near-global and hemispheric averaged PAs throughout all months. Compared to the CMIP3 (Bender et al. 2006), CMIP6/AMIP has better consistency in the difference in amplitude between the two peak values and the simulated phase. For the clear-sky PA (Fig. 4a), the simulated clear-sky PA is consistently lower than that of observation due to both hemispheres tend to underestimate the clear-sky PA during summers. Its maxima and minima in the NH are approximately 0.03 higher than those of the SH. The near-global averaged clear-sky PA also displays a bimodal pattern with a small amplitude and similar peak values indicating that the higher peak of the near-global averaged PA during boreal winter is mainly caused by the higher CAF. Indeed, Fig. 4b further shows that there are obvious CAF differences between models and observation, and between two hemispheres. In particular, the CAFs in the SH (or NH) range from 0.14 (0.12) to 0.16 (0.14). Figure 4a–c indicates that the discrepancy in the annual cycle of PA is mainly caused by the poor simulation of the CAF annual cycle. Meanwhile, the overestimation of the global averaged CAF persists throughout the entire annual cycle but

becomes relatively smaller during boreal winter than those of the other season, thus producing a much less variable annual cycle than the observation cycle.

To further investigate the discrepancy between the simulated and observed annual cycles, and check whether it can be attributed to specific climatic regions, Fig. 5a–f further describes the near-global distributions of observed amplitudes and corresponding amplitude ratios between the simulated and observed annual cycles of clear-sky PA, CAF and PA, respectively. Here, the amplitude is defined as the difference between maximum and minimum of albedo in the annual cycle (Stephens et al. 2015). The amplitude ratio is the ratio of the simulated to observed amplitude. If the ratio is greater than 1, the simulated amplitude is larger than that of observation. From Fig. 5c, we can see that the observed amplitudes of PA over the ocean are smaller than those values over land, its values range from approximately 0.04–0.20. This result is in agreement with the findings of Stephen et al. (2015). Over the tropics and subtropical regions, Fig. 5b and c show that the amplitudes of PA are primarily dominated by those of CAF, particularly over the ocean (Fig. 5a–c). Over the land regions of the middle latitudes in the NH, large amplitudes of clear-sky PA (> 0.3) occur in northern Europe, western Siberia, and parts of North America, thus further lead to large PA amplitudes over these regions. This may be related to the

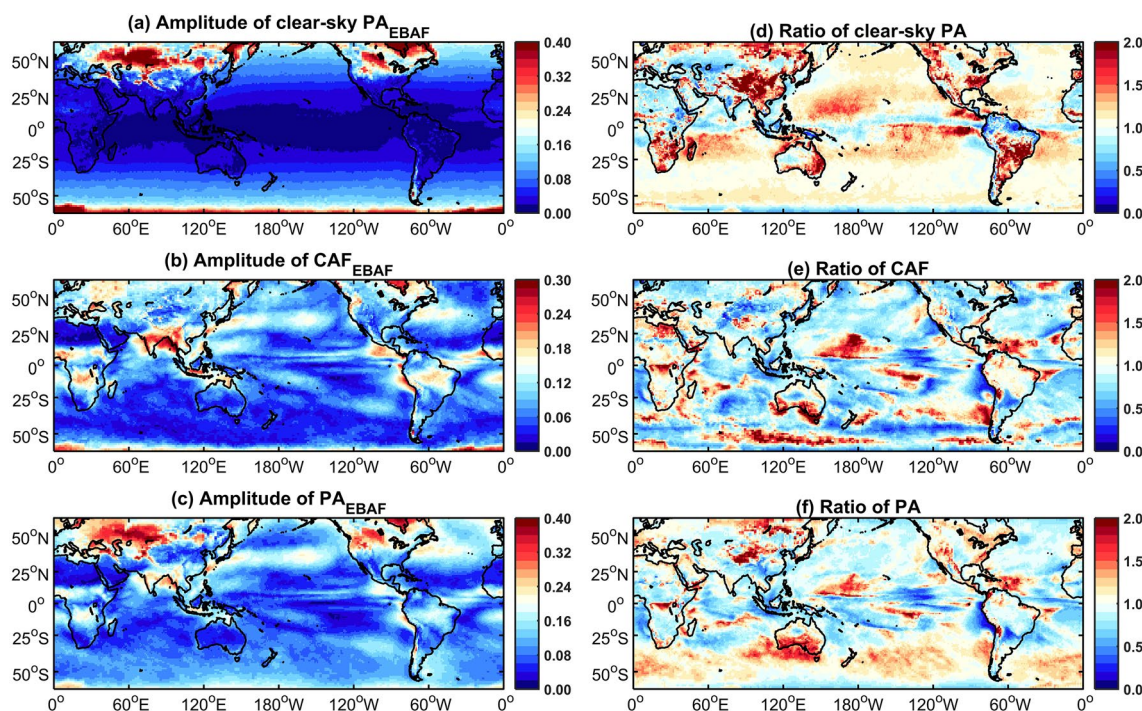


Fig. 5 Near-global distributions of the amplitude of the observed seasonal cycle of **a** clear-sky PA, **b** cloud albedo forcing and **c** PA, and its ratio of **d** clear-sky PA, **e** cloud albedo forcing and **f** PA between

the simulated and observed amplitude. The amplitude is the difference between maximum and minimum of albedo in its annual cycle

obvious seasonal changes of snow and ice covers across these regions. Compared to the observations, the MEM obviously overestimates the PA amplitudes over the subtropical central Pacific, the Southern Ocean and the TP (Fig. 5f). Furthermore, it strongly underestimates the PA amplitudes over some typical subtropical stratocumulus regions (i.e., the Canary Islands and Namibia). The bias is caused by the simulated cloud property errors in the models (Fig. 5e). Over the SH extratropical oceans (Fig. 5f), where are cloudy all the year round, however, surface errors are shown to be the main source of the overestimation of PA amplitudes over these regions, despite the cloud albedo forcing has nonnegligible contribution. This may be because the amplitudes of the clear-sky albedo are much larger than that of the CAF (Fig. 5a, b).

The near-global distributions of the phases (i.e., the month of maximum albedo) from the observed and simulated seasonal cycles of the clear-sky PA, CAF and PA are showed in Fig. 6a–f, respectively. For the clear-sky PA (Fig. 6a), the observed phases have obvious seasonality and land-sea differences. In the SH, the peak phases occur uniformly in June. In the NH, the peak phases occur in January (ocean) and December (land). For the observed phases of CAF (Fig. 6b), the results are more complex and fluctuating. In the SH, the peak phases mainly occur in summer. In contrast, the peak phases mainly occur during winter of the NH, except for the extratropical oceans and central Asia

(where the peak phases occur in summer) of NH. A previous study noted that the phase of reflected solar flux is affected by local changes in atmospheric and surface parameters (Stephen et al. 2015). Indeed, the phases of observed PA are affected synthetically by clear-sky PA and CAF (Fig. 6c). Over the extratropical oceans of SH and mid-latitude regions of NH, the clear-sky PA dominates the phase of PA, whereas the CAF dominates the phase of PA in the tropical regions. Although the simulated phases are similar to those observed values in terms of general spatial patterns, the spatial variations of the simulated phases are relatively weaker than those of observations (Fig. 6d–f). Compared to the observed PA phase, the MEM presents an obvious delay over the part of the NH extratropical central Pacific and the western part of the United States. For example, the simulated phase of PA mainly occurs in January, whereas the observed phase occurs in December over part of the NH extratropical central Pacific. This is mainly due to the poor simulation of the CAF phase over oceans.

3.2 Zonal mean biases and error contributions of different climatological regions

Figure 7a–c shows the 14-year zonal mean biases derived from MEM and CERES observations for the clear-sky PA, CAF and PA over ocean, land and globally, respectively. Figure 7a and c indicate that the global zonal mean bias is

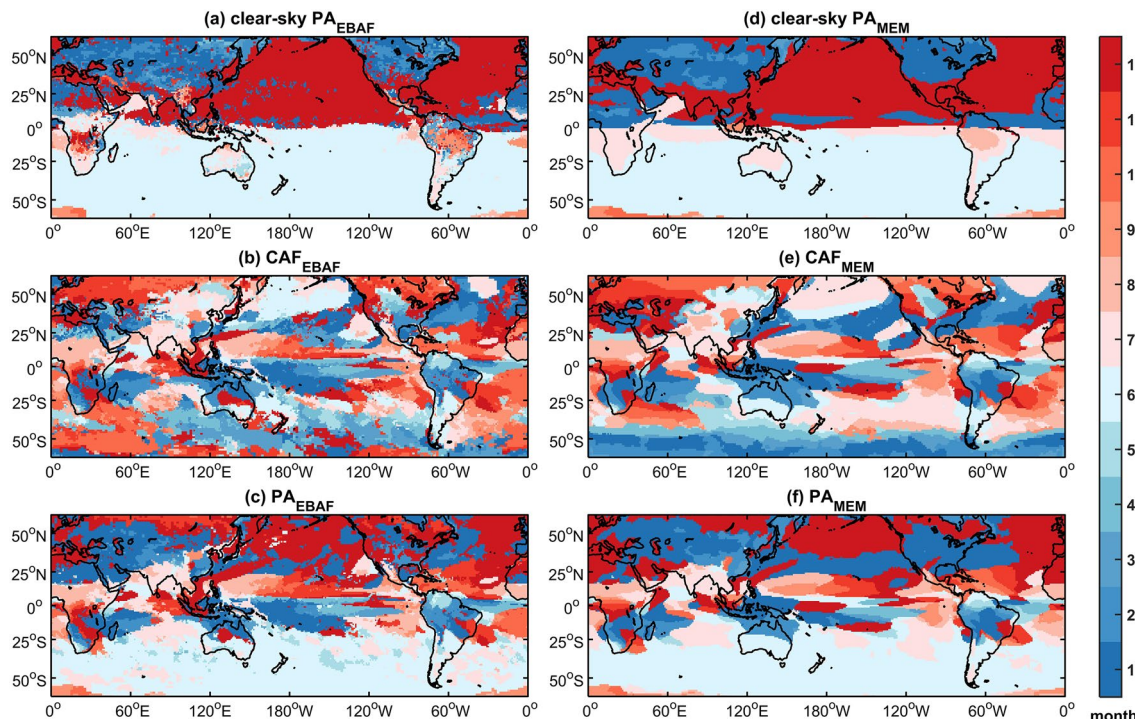


Fig. 6 Near-global distributions of the observed and simulated phase of the seasonal cycle for the **a, d** clear-sky PA, **b, e** cloud albedo forcing and **c, f** PA. The phase is the month of the maximum albedo

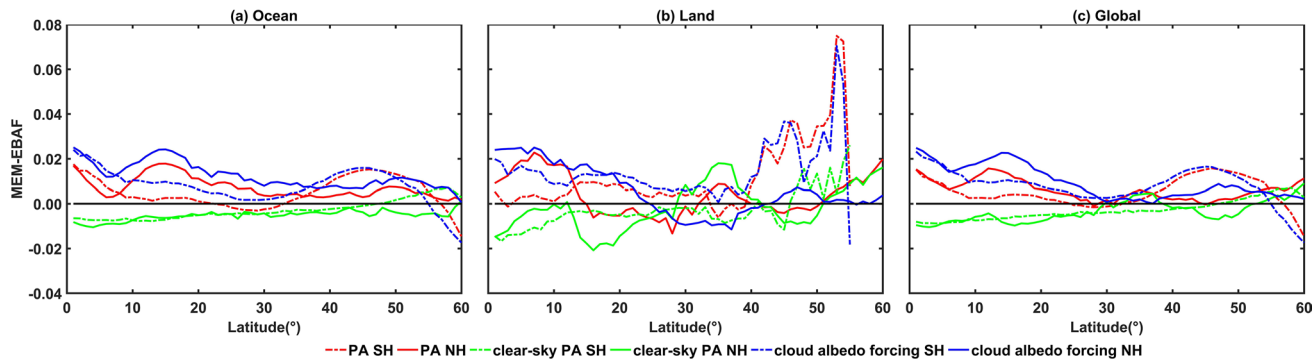


Fig. 7 Zonal averaged distributions of **a** Ocean, **b** land and **c** global clear-sky PA (green lines), cloud albedo forcing (blue lines) and PA (red lines) mean bias derived from MEM and CERES observations.

The solid lines show the results from NH, the dash lines show the results from SH

dominated by the vast ocean. For the ocean, both the CAF and clear-sky PA vary obviously with latitude, and the bias from the clear-sky PA is out of phase with the bias of the CAF. However, the zonal mean bias over the land experiences large variation without obvious latitudinal dependency. The large PA zonal mean bias of land is mainly located at the middle latitudes of the SH, and is caused by the poor simulation of cloud properties (Fig. 7b).

To comprehensively understand the albedo bias over the land, we further study the bias sources and demonstrate the sensitivity of regional albedo to different climatological regions. Five climatological regions are divided by the AI (see Sect. 2.3), and the global distribution of the AI is showed in Fig. S6. The time series of geographically weighted averaged clear-sky PA, CAF and PA mean biases over five climatological regions of the NH, SH and

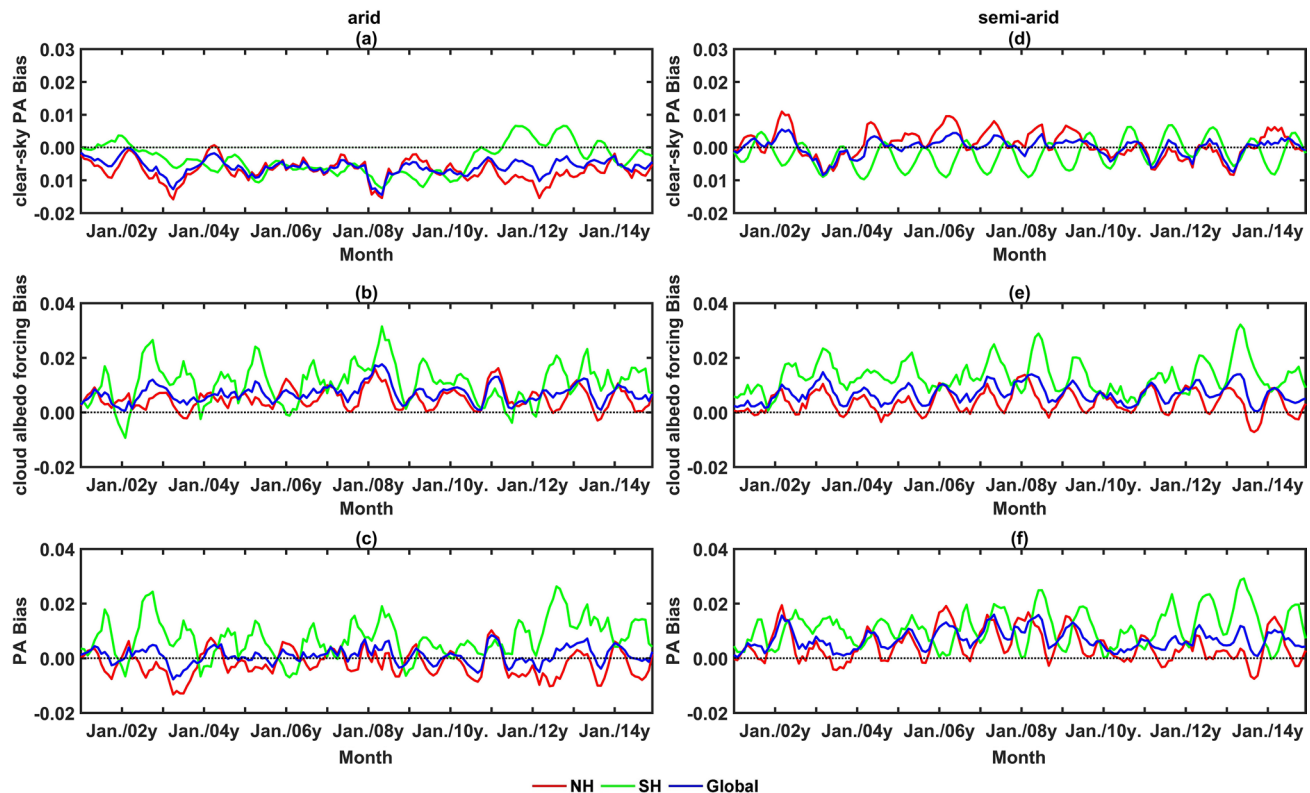


Fig. 8 The time series of regional averaged **a, d** clear-sky PA, **b, e** cloud albedo forcing and **c, f** PA biases between multimodel ensemble mean and satellite observations over arid and semi-arid regions. Here, red, green and blue lines represent NH, SH, and global, respectively

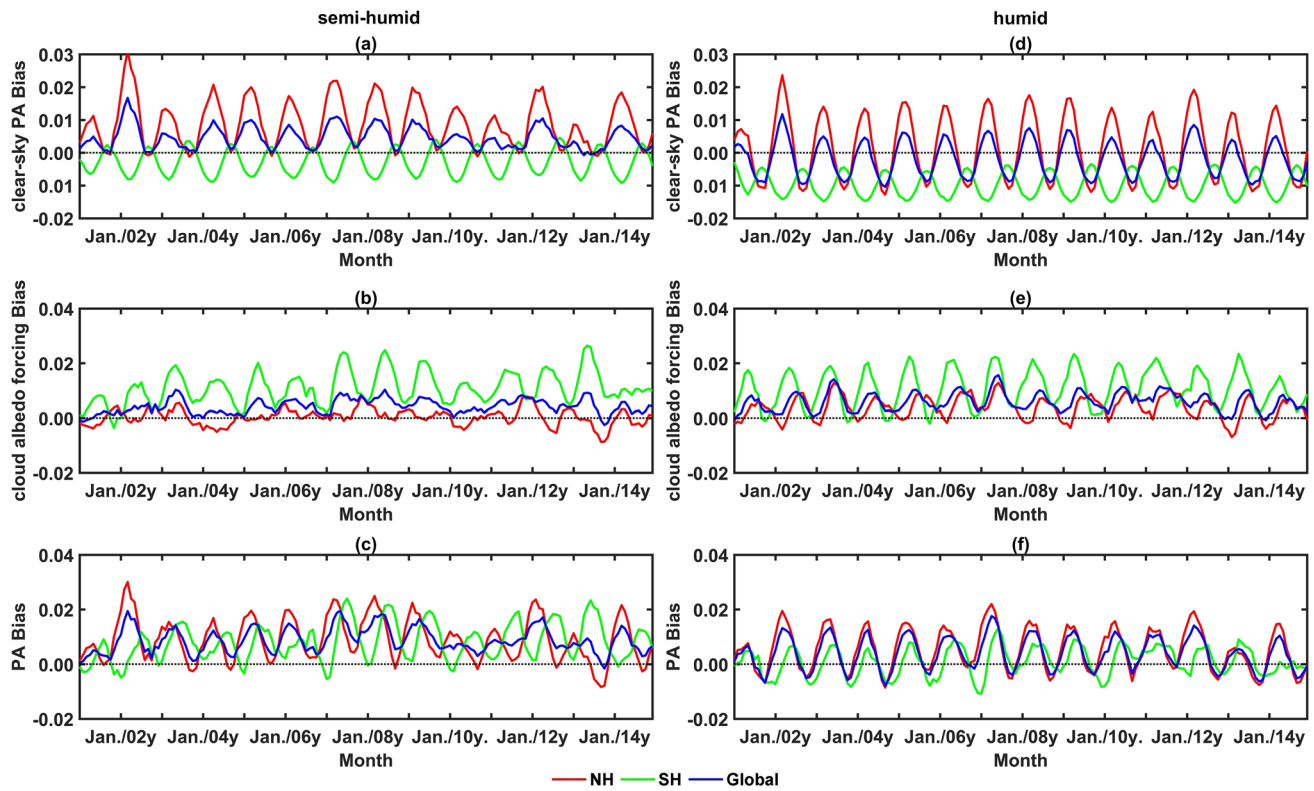


Fig. 9 Similar to Fig. 8 but for semi-humid and humid regions

globally are plotted in Fig. S7 and Figs. 8, 9, respectively. Note that the time series are filtered by performing 5-month smoothing.

As the hyper-arid regions (such as North Africa) are mainly located at the NH (see Fig. S7), the results of the SH are not shown. Certainly, the time series for the three variables over hyper-arid of NH and near-global almost overlap (see Fig. S7). The biases for the three variables all display significant seasonal variations. Obvious negative clear-sky PA biases and positive CAF biases exist in the NH. Due to the results of compensating biases, the biases of PA are small. This means that the simulation of clear-sky PA and CAF are limited, and the parameterization of PA needs to be improved in both the surface and cloud property simulations over hyper-arid regions. The main type of land cover is barren over North Africa, indicating that the bare soil albedo simulation is beneficial for simulating surface albedo, which strongly depends on the soil moisture content, surface roughness, and soil texture (Rechid et al. 2009).

For the arid regions, negative biases dominate the clear-sky PA biases of the NH, SH and global, whereas positive biases dominate the corresponding CAF biases. Similar to the results of hyper-arid regions, negative clear-sky PA biases and positive CAF biases offset each other and result in small PA biases (Fig. 8a–c). Compared to the arid regions of NH, the arid regions of SH (such as Australia) have much

larger CAF biases, indicating that the CAF is poorly simulated over there. The biases of two hemispheres cancel each other out, thus causing a much smaller variation in the PA bias time series. Semi-arid regions account for approximately 15% of the global land area and may represent the most sensitive regions to climate change due to their frail ecosystems (Huang et al. 2016a, 2017). Figure 8d–f shows that the clear-sky PA biases are much smaller than the CAF biases over semi-arid regions. Over these regions, previous studies found that the interplay between vegetation and the surface energy balance is complex. For example, in the case of vegetation cover increasing, enhanced water evaporation will reduce the local soil moisture, and further result in desertification. However, if the leaf areas become smaller, the increased surface albedo and decreased transpiration will aggravate the drought (Huang et al. 2017; Forzieri et al. 2017; Jian et al. 2018). In this study, the CAF biases of semi-arid regions are similar to those of arid regions, hence the PA biases are dominated by the positive CAF biases. Note that the positive PA biases are much smaller in hyper-arid and arid regions than those in semi-arid regions. The larger biases are masked in hyper-arid and arid regions due to the results of compensating biases. Considerable mineral dust particles are released from worldwide drylands. Huang et al. (2014) noted that dust-cloud interactions in dryland regions are complicated, as dust aerosols can affect the cloud

micro- and macro-physical processes (e.g., the liquid water path and cloud cover) in different ways (Huang et al. 2007, 2008). The improvement of dust-cloud interaction simulations is the key step to accurately simulate cloud albedo over drylands.

For the semi-humid regions (Fig. 9a–c), the positive clear-sky PA biases of the NH are much larger than those negative biases of the SH. The correlations of clear-sky PA biases between the NH and SH are high, and the NH and SH biases both reach their maximum and minimum values during boreal winter and boreal summer, respectively. The CAF biases of the NH are much smaller than those for the SH, indicating that the regional cloud simulation of the NH is much better than that of the SH. As the global clear-sky PA and CAF biases are almost positive, and the global positive PA biases are relatively larger compared to other areas. For the humid regions (Fig. 9d–f), it is clear that CAF biases for the SH are much larger than those for the NH. In the SH, the humid regions are mainly located in the Amazon, where the climate effect of absorbing aerosols (i.e., black carbon) from biomass burning has significant uncertainty in the model simulation. A previous study noted that the cloudiness response depends on the vertical distribution of smoke aerosols in the convective boundary layer of the Amazon's biomass burning regions

(Feingold et al. 2005). Additionally, Koren et al. (2008) found that increased smoking during biomass burning seasons can reduce cumulus cloud cover. However, the understanding of smoke-cloud interactions is still lacking, and thus makes the large uncertainties remain in models (Koch and Del Genio 2010).

Furthermore, we also provide the relative biases (RB, i.e., the absolute mean biases between models and observation divided by the observed mean value) of clear-sky PA, CAF and PA in five climatological regions for individual models (see Fig. 10). For the PA RBs, the PA near-global average RBs from MEM are greatest in semi-arid (2.2%) and semi-humid (2.8%) regions, whereas the PA RB from MEM in arid regions (0.3%) is smallest as a result of the compensating errors from CAF and clear-sky PA. Compared to humid regions, the PA RBs in dryland are much larger in some models (e.g., BCC-CESM2-MR, FGOALS-f3-L and GISS-E2-1-G). It is worth noting that the CAF RBs show a much larger spread in models compared to the corresponding clear-sky PA and PA relative biases. For the CAF RBs, the drylands exhibit much larger spread among the models compared to the humid regions, and can even reach to 150% in GISS-E2-1-G. The above results indicate that the simulation of mean value of CAF in drylands remains a challenge in CMIP6 models.

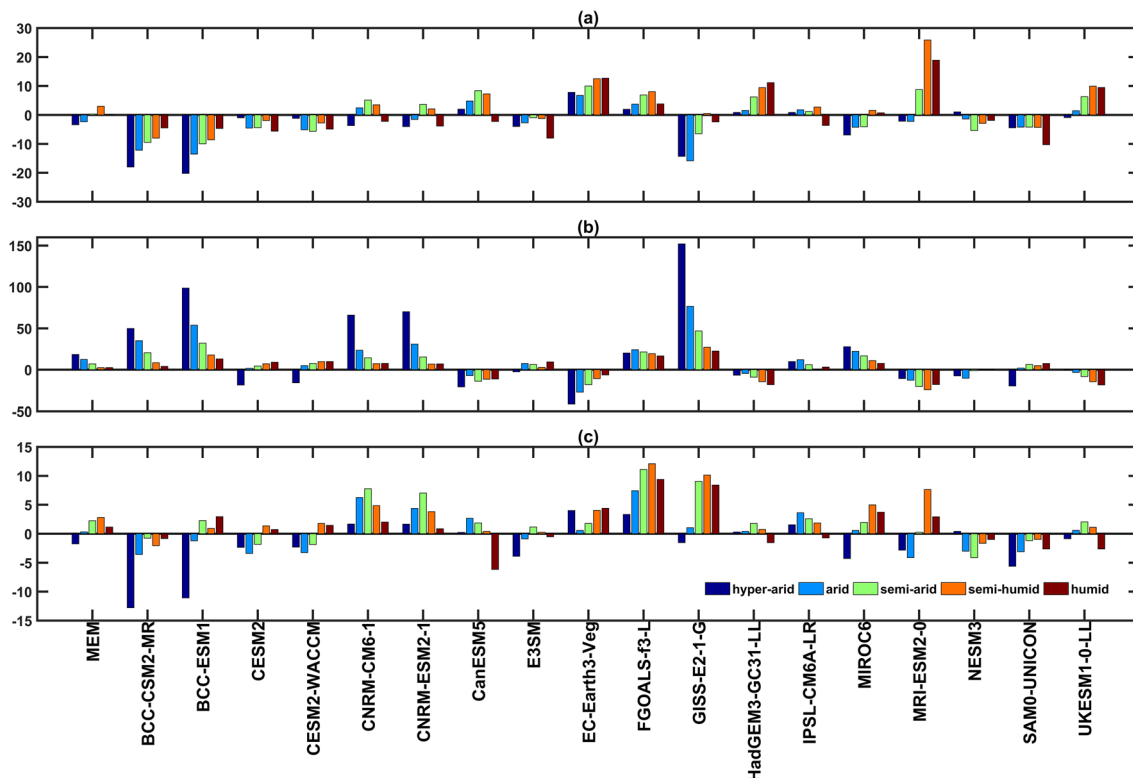


Fig. 10 Relative biases (%) of monthly averaged **a** clear-sky PA, **b** cloud albedo forcing and **c** PA between 19 models and satellite observations during 2001–2014 over different climatological regions

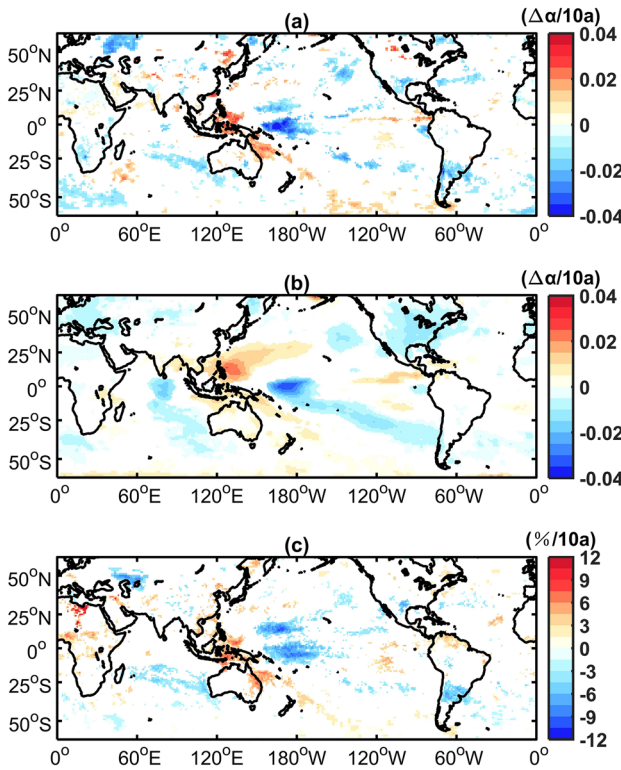


Fig. 11 Global distributions of PA trend from the **a** satellite observations (CERES EBAF) and **b** multimodel ensemble mean, and **c** the trend of daytime cloud fraction from satellite observations (CERES SSF) during 2001–2014. Those regions without values indicate that the trend is not significant at the 95% confidence level

3.3 Trends

The long-term trends of PA are also analyzed in this study. The global distributions of observed and simulated PA trends, and observed cloud fraction trends during daytime are given in Fig. 11a–c, respectively. Note that the trend analysis is based on deseasonalized time series and Sen's slope estimator (Ahani et al. 2012). We can see that the observed PA has significant positive and negative trends (95% confidence level) over the ocean off the northeastern coast of Australia and the South Pacific Convergence Zone (SPCZ), respectively (Fig. 11a). The similar pattern between

PA and cloud fraction trends (see Fig. 11a and c) indicates that the trends of PA are governed by the trends of the cloud fraction rather than those of the surface albedo (see Fig. S8). The models capture the significantly positive and negative PA trends well over the ocean off the northeastern coast of Australia and the SPCZ, however, they also simulate some unreal trends over ocean and land, especially over North America. Recently, Jian et al. (2018) found that the cloud fraction dominates the PA changes over most regions. The simulated unreal trend may be linked to the poor simulation of the cloud fraction variability. However, calculations of the cloud fraction in climate models link to various microphysical/dynamical processes and joined parameterizations and therefore construct the biggest immediate source of uncertainty in the model simulations (Wang and Su 2013). The improvements in cloud microphysical processes (e.g., condensation) and cloud overlap parameterization (Li et al. 2015) are bound to reduce the bias of PA simulation and enhance our confidence in climate projections.

Hemispheric symmetry is one of the important features of planetary albedo. This symmetry is achieved by more cloud reflection in the SH precisely offsetting the higher surface albedo in the NH. However, CMIP5 models can't recreate the observed hemispheric symmetry of the reflected flux (Stephens et al. 2015). Because the study area in our investigation is limited between 60°S and 60°N, the present study does not evaluate the performance of CMIP6 models in reproducing the hemispheric symmetry. Instead, we compare the observed and simulated trends of near-global and hemispheric PA during 2001–2014 (see Table 1). On the near-global scale, the simulated PA shows a weaker decreasing trend in all seasons compared to observation. The simulated largest decreasing trend occurs in DJF ($-0.0096/10a$), while the observed significant decreasing trends occur in MAM ($-0.0200/10a$) and SON ($-0.0152/10a$). The MEM can not reproduce the significant trends in MAM due to the models fail to capture the strong decreasing trend in NH ($-0.0330/10a$).

Finally, we also quantify the relative contribution rates of CAF and surface albedo (SA) anomalies to the long-term PA anomalies based on Eqs. (3–4). Figure 12a, b shows the global distributions of observed CAF contribution rates and

Table 1 The near-global and hemispheric averaged trends in observation and multimodel ensemble mean during 2001–2014. Note that the data are deseasonalized. The values in parentheses are results for

multimodel ensemble mean. The values showed in boldface indicate the trends are significant at the 95% confidence level

Trend of PA (unit: /10a)	Near-global (60° S–60° N)	NH (0°–60° N)	SH (0°–60° S)
March–May (MAM)	−0.0200 (-0.0075)	−0.0330 (-0.0066)	-0.0079 (-0.0108)
June–April (JJA)	-0.0039 (-0.0069)	-0.0063 (0.0016)	-0.0142 (-0.0115)
September–November (SON)	−0.0152 (-0.0052)	-0.0004 (-0.0086)	-0.0188 (-0.0005)
December–February (DJF)	-0.0102 (−0.0096)	0.0003 (-0.0064)	-0.0115 (-0.0101)
Annual	−0.0117 (−0.0069)	-0.0096 (-0.0052)	−0.0155 (-0.0065)

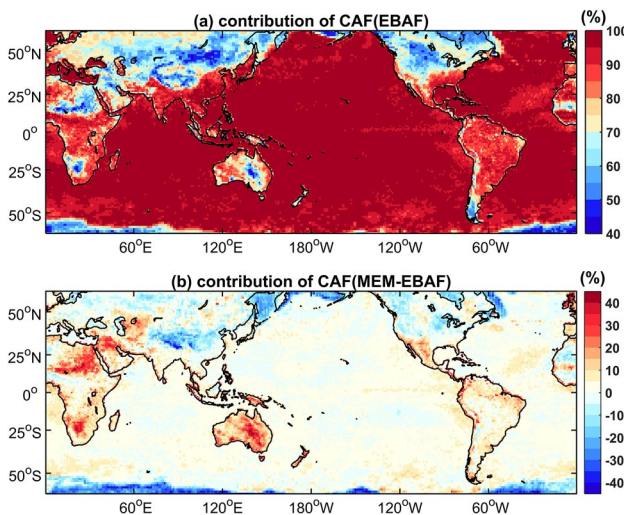


Fig. 12 Near-global distributions of the relative contributions of cloud albedo forcing to PA from the **a** CERES satellite observations and its **b** difference between multimodel ensemble mean and observations from 2001 to 2014. Note that the anomalies are deseasonalized and detrend

its differences between the MEM and CERES EBAF, respectively. Figure 12a clearly shows that the long-term variations in PA are dominated by changes in the CAF, and the CAF contribution rates are greater than 90% in most regions. This result is consistent with a recent study from Jian et al. (2018), who proved that the cloud properties dominate the PA changes in middle and low latitudes. Compared to the observation, the MEM considerably overestimates the CAF contribution in the middle latitudes land regions, particularly over Australia and North Africa. Furthermore, the MEM obviously underestimates the CAF contribution over the TP and the western United States. Note that these regions are typical arid or semi-arid regions, indicating that cloud and surface simulations in drylands are still challenging. Under the TP warming background, Shen et al. (2015) suggested that regional vegetation greening is being detected as a response, indicating that variation in surface albedo would be strengthened over the TP. Even so, the contributions of surface albedo may be obviously overestimated.

4 Conclusions and discussion

The Earth's planetary albedo (PA) has an essential impact on the global energy budget. To better predict climate change, it is thus necessary to make a comprehensive assessment of PA for the current CMIP models by using long-term observation data. This study investigates the ability of CMIP6/AMIP models in reproducing the observed near-global and regional planetary albedos based on 14 years of monthly data (2001–2014) from the CERES EBAF Ed4.1 dataset

and the CMIP6 GCMs AMIP outputs. We analyze the near-global and regional biases of the simulated PA, including its inter-month variation and annual cycle, the model uncertainties in different climatological regions and the trend biases. The results indicate that some persistent biases in the previous models persist in the CMIP6 models; however, some progresses have been made in recent years.

(1) Statistical results show that the large negative correlations of PA between model ensemble mean and observation are addressed over the subtropical stratocumulus regions, however, the model still underestimates the PA there. In addition, compared to CMIP5 models, the CMIP6 models continue to overestimate the PA/CAF over the tropical oceans.

(2) Compared to satellite observations, the model ensemble mean exhibits superior reproducibility in simulating the seasonal changes in the near-global averaged clear-sky PA but fails to reproduce the cloud albedo forcing well, thereby causing the overestimation of the PA. The biases have persisted from CMIP3 (Stephens et al. 2015). However, for the annual cycles, the MEM captures the difference in amplitude between the two peak values of PA well. The simulated phase of the annual cycle agrees well with that of observations. Furthermore, the seasonal discrepancy in the PA bias is mainly caused by the systematic overestimation of the CAF.

(3) By analyzing the ocean and land zonal mean biases, we find that the ocean zonal mean biases dominate the albedo zonal mean biases. For land, the zonal mean bias experiences considerable variation without statistical latitudinal dependency. Based on the AI, we find that the PA relative bias is greatest in semi-arid (2.2%) and semi-humid (2.8%) regions, whereas its relative PA bias in arid regions (0.3%) is smallest as a result of compensating errors in the CAF and clear-sky PA simulations.

(4) The MEM can capture the long-term trends of PA well over the ocean off the northeastern coast of Australia and the SPCZ; however, it simulates some unreal trends over ocean and land, which are linked to the poor cloud fraction simulation. The better parameterization of cloud overlap properties is needed to improve the cloud fraction simulation and following PA simulation.

Although cloud biases dominate the PA biases, surface albedo biases also play a non-negligible role. In the past few decades, the Earth becomes significantly warm, hence accelerates the increase of the leaf area of vegetation. Recent studies (Chen et al. 2019; Yao et al. 2019) have shown a vegetation greening pattern that is strikingly prominent in China. This “greening Earth” can influence Earth's surface process and resource ecology, hence influencing the energy budget. This means that the parameterization of vegetation type, especially the LAI, needs to be highlighted in climate models in response to a greening Earth. Different from the

CAF, the CMIP6 still struggles to simulate the multiyear annual mean surface albedo over drylands and the improvement is quite modest. The snow cover, DSA and vegetation cover thus need to be received more attention for improving the parameterization of surface albedo and corresponding clear-sky albedo.

The trends in the CMIP6 that coupled historical outputs with free-running are rather different from those obtained from the AMIP simulation and fail to reproduce the significant trends of PA (not shown). It means that the large biases from trends in the coupled models are mainly attributable to the biases in the SST and related circulations rather than the cloud processes. To find out the potential sources about the divergences of PA in model simulations, the comparison of cloud (or surface) properties between models and observations should be performed more reasonably. On the one hand, satellite retrieval algorithms of cloud (or surface) properties and potential uncertainties need to be further improved and reduced (Zhao et al. 2012, 2014), especially for those regions with few observations (e.g., the TP) (Zhao et al. 2016; Letu et al. 2018). On the other hand, cloud simulators are needed to be embedded into more CMIP6 models to evaluate the simulated cloud properties and related physical processes in future research (Stouffer et al. 2017). In addition, observational evidence shows that the long-term variation of PA is closely controlled by the cloud properties, especially the cloud fraction (Jian et al. 2018). Recent studies have indicated that cloud overlap parameterization based on the dynamical factors is helpful to improve the calculation of cloud fraction in the model (Li et al. 2018; Li et al. 2019). Therefore, it is clear that related parameterizations of cloud properties should also be further improved and developed in the models to reduce the PA bias in models.

Acknowledgements This work was supported by the Strategic Priority Research Program of the Chinese Academy of Sciences (XDA2006010301), the Innovative Research Groups of the National Science Foundation of China (41521004), the National Science Foundation of China (41575015), and the Fundamental Research Funds for the Central Universities (Lzujbky-2017-64).

References

- Bao S et al (2018) Spatiotemporal distributions of cloud parameters and the temperature response over the mongolian plateau during 2006–2015 based on MODIS data. *IEEE J-Stars* 12:549–558. <https://doi.org/10.1109/JSTARS.2018.2857827>
- Bender FAM, Rodhe H, Charlson RJ, Ekman AML, Loeb N (2006) 22 views of the global albedo—comparison between 20 GCMs and two satellites. *Tellus A* 58:320–330. <https://doi.org/10.1111/j.1600-0870.2006.00181.x>
- Bender FAM, Engstrom A, Karlsson J (2016) Factors controlling cloud albedo in marine subtropical stratocumulus regions in climate models and satellite observations. *J Clim* 29:3559–3587. <https://doi.org/10.1175/JCLI-D-15-0095.1>
- Boucher O et al (2013) Clouds and aerosols. In: Stocker TF, Qin D, Plattner G-K, Tignor M, Allen SK, Boshung J, Naules A, Xia Y, Bex V, Midgley PM (eds) Climate change 2013: the physical science basis. Contribution of working group I to the fifth assessment report of the intergovernmental panel on climate change. Cambridge University Press, Cambridge
- Chen C et al (2019) China and India lead in greening of the world through land-use management. *Nat Sustain* 2:122. <https://doi.org/10.1038/s41893-019-0220-7>
- Doelling DR et al (2013) Geostationary enhanced temporal interpolation for CERES flux products. *J Atmos Ocean Technol* 30:1072–1090. <https://doi.org/10.1175/JTECH-D-12-00136.1>
- Donohoe A, Battisti DS (2011) Atmospheric and surface contributions to planetary Albedo. *J Clim* 24:4402–4418. <https://doi.org/10.1175/2011JCLI3946.1>
- Eyring V, Bony S, Meehl GA, Senior CA, Stevens B, Stouffer RJ, Taylor KE (2016) Overview of the coupled model intercomparison project phase 6 (CMIP6) experimental design and organization. *Geosci Model Dev* 9:1937–1958. <https://doi.org/10.5194/gmd-9-1937-2016>
- Fan T et al (2018a) Emission or atmospheric processes? An attempt to attribute the source of large bias of aerosols in eastern China simulated by global climate models. *Atmos Chem Phys* 18:1395–1417. <https://doi.org/10.5194/acp-18-1395-2018>
- Fan T et al (2018b) Quantify contribution of aerosol errors to cloud fraction biases in CMIP5 atmospheric model Intercomparison project simulations. *Int J Climatol* 38:3140–3156. <https://doi.org/10.1002/joc.5490>
- Feingold G, Jiang HL, Harrington JY (2005) On smoke suppression of clouds in Amazonia. *Geophys Res Lett* 32:L02804. <https://doi.org/10.1029/2004gl021369>
- Feng S, Fu Q (2013) Expansion of global drylands under a warming climate. *Atmos Chem Phys* 13:10081–10094. <https://doi.org/10.5194/acp-13-10081-2013>
- Forzieri G, Alkama R, Miralles DG, Cescatti A (2017) Satellites reveal contrasting responses of regional climate to the widespread greening of Earth. *Science* 356:1180–1184. <https://doi.org/10.1126/science.aal1727>
- Fu Q, Feng S (2014) Responses of terrestrial aridity to global warming. *J Geophys Res-Atmos* 119:7863–7875. <https://doi.org/10.1002/2014JD021608>
- Fu Q, Cribb MC, Barker HW, Krueger SK, Grossman A (2000) Cloud geometry effects on atmospheric solar absorption. *J Atmos Sci* 57:1156–1168. [https://doi.org/10.1175/1520-0469\(2000\)057%3c1156:CGEOAS%3e2.0.CO;2](https://doi.org/10.1175/1520-0469(2000)057%3c1156:CGEOAS%3e2.0.CO;2)
- Gleckler PJ, Taylor KE, Doutriaux C (2008) Performance metrics for climate models. *J Geophys Res-Atmos* 113:D06104. <https://doi.org/10.1029/2007JD008972>
- Govaerts YM, Pereira JM, Pinty B, Mota B (2002) Impact of fires on surface albedo dynamics over the African continent. *J Geophys Res-Atmos* 107:4629. <https://doi.org/10.1029/2002jd002388>
- Houghton JT et al (2001) Climate change 2001: the scientific basis. Contribution of working group I to the third assessment report of the intergovernmental panel on climate change. Cambridge University Press, Cambridge
- Hu Y, Stamnes K (1993) An accurate parameterization of the radiative properties of water clouds suitable for use in climate models. *J Clim* 6:728–742. [https://doi.org/10.1175/1520-0442\(1993\)006%3c0728:APOTR%3e2.0.CO;2](https://doi.org/10.1175/1520-0442(1993)006%3c0728:APOTR%3e2.0.CO;2)
- Hu Y, Stamnes K (2000) Climate sensitivity to cloud optical properties. *Tellus B* 52:81–93. <https://doi.org/10.1034/j.1600-0889.2000.00993.x>
- Huang J, Yi Y (1991) Inversion of a nonlinear dynamical model from the observation. *Sci China B* 34:1246–1246

- Huang J et al (2007) Summer dust aerosols detected from CALIPSO over the Tibetan Plateau. *Geophys Res Lett* 34:L18805. <https://doi.org/10.1029/2007GL029938>
- Huang J et al (2008) Long-range transport and vertical structure of Asian dust from CALIPSO and surface measurements during PACDEX. *J Geophys Res-Atmos* 113:D23212. <https://doi.org/10.1029/2008JD010620>
- Huang J, Guan X, Ji F (2012) Enhanced cold-season warming in semi-arid regions. *Atmos Chem Phys* 12:5391–5398. <https://doi.org/10.5194/acp-12-5391-2012>
- Huang J, Wang T, Wang W, Li Z, Yan H (2014) Climate effects of dust aerosols over East Asian arid and semiarid regions. *J Geophys Res-Atmos* 119:11398–11416. <https://doi.org/10.1002/2014JD021796>
- Huang J, Ji M, Xie Y, Wang S, He Y, Ran J (2016a) Global semi-arid climate change over last 60 years. *Clim Dyn* 46:1131–1150. <https://doi.org/10.1007/s00382-015-2636-8>
- Huang J, Yu H, Guan X, Wang G, Guo R (2016b) Accelerated dryland expansion under climate change. *Nat Clim Chang* 6:166. <https://doi.org/10.1038/Nclimate2837>
- Huang J et al (2017) Dryland climate change: Recent progress and challenges. *Rev Geophys* 55:719–778. <https://doi.org/10.1002/2016rg000550>
- Ichoku C et al (2016) Biomass burning, land-cover change, and the hydrological cycle in Northern sub-Saharan Africa. *Environ Res Lett* 11:095005. <https://doi.org/10.1088/1748-9326/11/9/095005>
- Jian B, Li J, Wang G, He Y, Han Y, Zhang M, Huang J (2018) The impacts of atmospheric and surface parameters on long-term variations in the planetary Albedo. *J Clim* 31:8705–8718. <https://doi.org/10.1175/JCLI-D-17-0848.S1>
- Kato S et al (2018) Surface irradiances of edition 4.0 clouds and the Earth's radiant energy system (CERES) energy balanced and filled (EBAF) data product. *J Clim* 31:4501–4527. <https://doi.org/10.1175/JCLI-D-17-0523.1>
- Koch D, Del Genio AD (2010) Black carbon semi-direct effects on cloud cover: review and synthesis. *Atmos Chem Phys* 10:7685–7696. <https://doi.org/10.5194/acp-10-7685-2010>
- Koren I, Martins JV, Remer LA, Afargan H (2008) Smoke invigoration versus inhibition of clouds over the Amazon. *Science* 321:946–949. <https://doi.org/10.1126/science.1159185>
- Lauer A, Hamilton K (2013) Simulating clouds with global climate models: a comparison of CMIP5 results with CMIP3 and satellite data. *J Clim* 26:3823–3845. <https://doi.org/10.1175/JCLI-D-12-00451.1>
- Lauer A et al (2017) Benchmarking CMIP5 models with a subset of ESA CCI Phase 2 data using the ESMValTool. *Remote Sens Environ* 203:9–39. <https://doi.org/10.1016/j.rse.2017.01.007>
- Letu H et al (2018) Ice cloud properties from Himawari-8/AHI next-generation geostationary satellite: capability of the AHI to monitor the DC cloud generation process. *IEEE T Geosci Remote* 57:3229–3239. <https://doi.org/10.1109/TGRS.2018.2882803>
- Li J, Huang J, Starnes K, Wang T, Lv Q, Jin H (2015) A global survey of cloud overlap based on CALIPSO and CloudSat measurements. *Atmos Chem Phys* 15:519–536. <https://doi.org/10.5194/acp-15-519-2015>
- Li Y, Wang T, Zeng ZZ, Peng SS, Lian X, Piao SL (2016) Evaluating biases in simulated land surface albedo from CMIP5 global climate models. *J Geophys Res-Atmos* 121:6178–6190. <https://doi.org/10.1002/2016JD024774>
- Li J, Lv Q, Zhang M, Wang T, Kawamoto K, Chen S, Zhang B (2017) Effects of atmospheric dynamics and aerosols on the fraction of supercooled water clouds. *Atmos Chem Phys* 17:1847–1863. <https://doi.org/10.5194/acp-17-1847-2017>
- Li J et al (2018) The impact of atmospheric stability and wind shear on vertical cloud overlap over the Tibetan Plateau. *Atmos Chem Phys* 18:7329–7343. <https://doi.org/10.5194/acp-18-7329-2018>
- Li J, Jian B, Zhao C, Zhao Y, Wang J, Huang J (2019) Atmospheric instability dominates the long-term variation of cloud vertical overlap over the Southern Great Plains site. *J Geophys Res-Atmos* 124:9691–9701. <https://doi.org/10.1029/2019JD030954>
- Loeb NG, Wielicki BA, Rose FG, Doelling DR (2007) Variability in global top-of-atmosphere shortwave radiation between 2000 and 2005. *Geophys Res Lett* 34:L03704. <https://doi.org/10.1029/2006gl028196>
- Loeb NG, Manalo-Smith N, Su WY, Shankar M, Thomas S (2016) CERES top-of-atmosphere earth radiation budget. Climate data record: accounting for in-orbit changes in instrument calibration. *Remote Sens* 18:182. <https://doi.org/10.3390/rs8030182>
- Maidment DR (1993) Handbook of hydrology, vol 9780070. McGraw-Hill, New York
- McCoy DT et al (2015) Natural aerosols explain seasonal and spatial patterns of Southern Ocean cloud albedo. *Sci Adv* 1:e1500157. <https://doi.org/10.1126/sciadv.1500157>
- Middleton N, Thomas D (1997) World Atlas of desertification. Edward Arnold, London
- Myhre G, Hoyle CR, Berglen TF, Johnson BT, Haywood JM (2008) Modeling of the solar radiative impact of biomass burning aerosols during the Dust and Biomass-burning Experiment (DABEX) *J Geophys Res-Atmos* 113:D00C16. <https://doi.org/10.1029/2008jd009857>
- Nam C, Bony S, Dufresne JL, Chepfer H (2012) The ‘too few, too bright’ tropical low-cloud problem in CMIP5 models. *Geophys Res Lett* 39:L21801. <https://doi.org/10.1029/2012gl053421>
- Pallé E, Goode P, Montanes-Rodriguez P, Koonin S (2004) Changes in Earth’s reflectance over the past two decades. *Science* 304:1299–1301. <https://doi.org/10.1126/science.1094070>
- Qu X, Hall A (2005) Surface contribution to planetary albedo variability in cryosphere regions. *J Clim* 18:5239–5252. <https://doi.org/10.1175/JCLI3555.1>
- Rechid D, Raddatz T, Jacob D (2009) Parameterization of snow-free land surface albedo as a function of vegetation phenology based on MODIS data and applied in climate modelling. *Theor Appl Climatol* 95:245–255. <https://doi.org/10.1007/s00704-008-0003-y>
- Shen M et al (2015) Evaporative cooling over the Tibetan Plateau induced by vegetation growth. *Proc Natl Acad Sci USA* 112:9299–9304. <https://doi.org/10.1073/pnas.1504418112>
- Solomon S et al (2007) The physical science basis: contribution of working group I to the fourth assessment report of the Intergovernmental Panel on Climate Change Intergovernmental Panel on Climate Change (IPCC), Climate change 2007. Cambridge University Press, Cambridge
- Stephens GL, O’Brien D, Webster PJ, Pilewski P, Kato S, Li JL (2015) The albedo of earth. *Rev Geophys* 53:141–163. <https://doi.org/10.1002/2014RG000449>
- Stocker TF et al (2013) Climate change 2013: the physical science basis contribution of working group I to the fifth assessment report of the intergovernmental panel on climate change. Cambridge University Press, Cambridge
- Stouffer RJ, Eyring V, Meehl GA, Bony S, Senior C, Stevens B, Taylor KE (2017) CMIP5 scientific gaps and recommendations for CMIP6. *B Am Meteorol Soc* 98:95–105. <https://doi.org/10.1175/bams-d-15-00013.1>
- Tsushima Y et al (2006) Importance of the mixed-phase cloud distribution in the control climate for assessing the response of clouds to carbon dioxide increase: a multi-model study. *Clim Dyn* 27:113–126. <https://doi.org/10.1007/s00382-006-0127-7>
- Van Weverberg K et al (2018) CAUSES: attribution of surface radiation biases in NWP and climate models near the US Southern Great Plains. *J Geophys Res-Atmos* 123:3612–3644. <https://doi.org/10.1002/2017jd027188>
- Vignesh PP, Jiang JH, Kishore P, Su H, Smay T, Brighton N, Velicogna I (2020) Assessment of CMIP6 cloud fraction and comparison

- with satellite observations. *Earth Space Sci* 7:e2019EA000975. <https://doi.org/10.1029/2019EA000975>
- Voigt A, Stevens B, Bader J, Mauritsen T (2014) Compensation of hemispheric albedo asymmetries by shifts of the ITCZ and tropical clouds. *J Clim* 27:1029–1045. <https://doi.org/10.1175/JCLI-D-13-00205.1>
- Wang H, Su W (2013) Evaluating and understanding top of the atmosphere cloud radiative effects in Intergovernmental Panel on Climate Change (IPCC) Fifth Assessment Report (AR5) Coupled Model Intercomparison Project Phase 5 (CMIP5) models using satellite observations. *J Geophys Res-Atmos* 118:683–699. <https://doi.org/10.1029/2012jd018619>
- Wang Y, Zhao C (2017) Can MODIS cloud fraction fully represent the diurnal and seasonal variations at DOE ARM SGP and Manus sites? *J Geophys Res-Atmos* 122:329–343. <https://doi.org/10.1002/2016JD025954>
- Wilcox EM (2010) Stratocumulus cloud thickening beneath layers of absorbing smoke aerosol. *Atmos Chem Phys* 10:11769–11777. <https://doi.org/10.5194/acp-10-11769-2010>
- Xie S, Liu X, Zhao C, Zhang Y (2013) Sensitivity of CAM5-simulated Arctic clouds and radiation to ice nucleation parameterization. *J Clim* 26:5981–5999. <https://doi.org/10.1175/JCLI-D-12-00517.1>
- Xu H et al (2017) Warming effect of dust aerosols modulated by overlapping clouds below. *Atmos Environ* 166:393–402. <https://doi.org/10.1016/j.atmosenv.2017.07.036>
- Yang Y, Zhao C, Fan H (2020) Spatiotemporal distributions of cloud properties over China based on Himawari-8 advanced Himawari imager data. *Atmos Res* 240:104927. <https://doi.org/10.1016/j.atmosres.2020.104927>
- Yao R, Wang L, Huang X, Chen X, Liu Z (2019) Increased spatial heterogeneity in vegetation greenness due to vegetation greening in mainland China. *Ecol Indic* 99:240–250. <https://doi.org/10.1016/j.ecolind.2018.12.039>
- Zhao C, Klein SA, Xie S, Liu X, Boyle JS, Zhang Y (2012) Aerosol first indirect effects on non-precipitating low-level liquid cloud properties as simulated by CAM5 at ARM sites. *Geophys Res Lett* 39:L08806. <https://doi.org/10.1029/2012gl051213>
- Zhao C, Xie S, Chen X, Jensen MP, Dunn M (2014) Quantifying uncertainties of cloud microphysical property retrievals with a perturbation method. *J Geophys Res-Atmos* 119:5375–5385. <https://doi.org/10.1002/2013JD021112>
- Zhao C, Liu L, Wang Q, Qiu Y, Wang W, Wang Y, Fan T (2016) Toward understanding the properties of high ice clouds at the Naqu site on the Tibetan Plateau using ground-based active remote sensing measurements obtained during a short period in July 2014. *J Appl Meteorol Climatol* 55:2493–2507. <https://doi.org/10.1016/j.atmosres.2017.02.002>
- Zhao C, Chen Y, Li J, Letu H, Su Y, Chen T, Wu X (2019) Fifteen-year statistical analysis of cloud characteristics over China using terra and aqua moderate resolution imaging spectroradiometer observations. *Int J Climatol* 39:2612–2629. <https://doi.org/10.1002/joc.5975>

Publisher's Note Springer Nature remains neutral with regard to jurisdictional claims in published maps and institutional affiliations.